

Ground Plane Polling for 6DoF Pose Estimation of Objects on the Road

Akshay Rangesh and Mohan M. Trivedi

Laboratory for Intelligent & Safe Automobiles, UC San Diego

{arangesh, mtrivedi}@ucsd.edu

Abstract

This paper introduces an approach to produce accurate 3D detection boxes for objects on the ground using single monocular images. We do so by merging 2D visual cues, 3D object dimensions, and ground plane constraints to produce boxes that are robust against small errors and incorrect predictions. First, we train a single-shot convolutional neural network (CNN) that produces multiple visual and geometric cues of interest: 2D bounding boxes, 2D keypoints of interest, coarse object orientations and object dimensions. Subsets of these cues are then used to poll probable ground planes from a pre-computed database of ground planes, to identify the “best fit” plane with highest consensus. Once identified, the “best fit” plane provides enough constraints to successfully construct the desired 3D detection box, without directly predicting the 6DoF pose of the object. The entire ground plane polling (GPP) procedure is constructed as a non-parametrized layer of the CNN that outputs the desired “best fit” plane and the corresponding 3D keypoints, which together define the final 3D bounding box. This single-stage, single-pass CNN results in superior localization compared to more complex and computationally expensive approaches.

1. Introduction

Localizing objects in 3D is of extreme importance in autonomous driving and driver safety applications. Traditional and contemporary approaches have mostly relied on range sensors like LiDARs and Radars, or stereo camera pairs to predict the desired 6DoF pose and dimensions of objects of interest. Some of these approaches are demonstrably robust under a variety of conditions, and produce high quality 3D detection boxes despite large occlusions, truncations etc. However, the benefits of 3D sensors are almost always accompanied by certain downsides. These sensors are typically orders of magnitudes more expensive

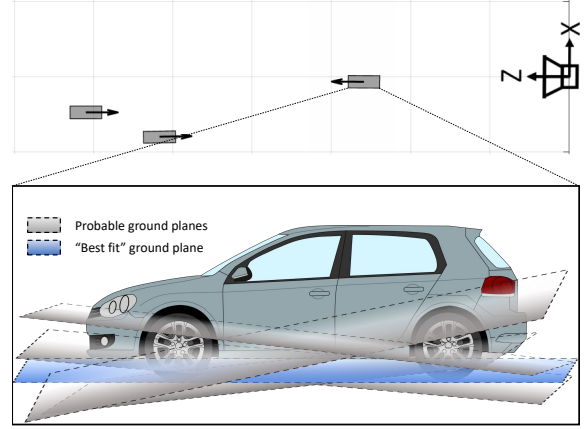


Figure 1: Illustration of the ground plane constraint enforced in this study. Each object is assumed to lie on one of many probable ground plane configurations, termed to be the “best fit” plane associated with the object.

compared to cheap cameras, and are also bulkier and power-hungry. It is therefore desirable to carry out 3D object detection with monocular cameras, if suitable robustness can be achieved. A robust 3D detector could also in turn improve the performance of purely camera based tracking [1] and prediction [2] systems. This however introduces many challenges, most of which stem from the fact that predicting 3D attributes from 2D measurements is an ill-posed problem.

In this study, we overcome this challenge by only considering those cues (visual or otherwise), that can be reliably predicted using monocular camera images alone, while also being generalizable to data captured by cameras with different settings and parameters. With this in mind, we only predict attributes like 2D detection boxes, 2D keypoint locations, coarse local orientations, and dimensions of the object in 3D. State-of-the-art approaches for predicting 2D attributes like detection boxes and keypoints are known to generalize quite well to new datasets and scenarios. On the other hand, coarse local orientations are closely tied to the

[†]Code: <https://github.com/arangesh/Ground-Plane-Polling>

appearance of an object, and can be reliably predicted as we will show later. Finally, the dimensions of an object in 3D are somewhat tied to the appearance of an object (e.g. cars, vans, trucks etc. look different), but are less prone to large errors because of the low variance in dimensions of an object within a particular object class.

On the other hand, we would like the constraints and assumptions we enforce to result in reasonable estimates, while not being too restrictive. Ground plane constraints are a common choice, where objects of interest are forced to lay on a common plane. This however, might be too restrictive of an assumption, resulting in large errors for objects farther away lying on irregular terrains. In this study, we instead create a database of probable ground planes, and choose the “best fit” plane for each object locally (see Figure 1). This is similar to modeling the road terrain with a piecewise planar approximation, thereby loosening the single ground plane constraint. We also purposefully predict more attributes than needed to estimate a 3D detection box, and use these predictions to form maximal *consensus set* of attributes, in a manner similar to traditional RANSAC approaches. This makes our approach robust to individual errors and outliers in predictions.

Our main contributions in this work can be summarized as follows - 1) We propose a single-shot approach to predict the 6DoF pose and dimensions of objects on the road by predicting 2D attributes of interest in single monocular images. 2) We then combine subsets of these attributes to robustly identify the “best fit” ground plane for each object locally using a novel polling approach, thereby determining the 3D detection box corresponding to each object. 3) Finally, we carry out extensive comparisons and experiments with previous state-of-the-art techniques to illustrate the advantages and limitations of our approach.

2. Related Research

With the introduction of new large-scale datasets like [3–5] and overall success of CNNs, many approaches for 3D object detection and 6DoF pose estimation using single monocular images have recently emerged. Although these methods are mostly based on popular 2D detection architectures [6–9], they differ in the ways they incorporate 3D information, the attributes they predict, and the constraints they enforce.

Xiang et al. [10] cluster the set of possible object poses into viewpoint-dependent subcategories using 3D voxel patterns. In their following work [11], these subcategories were used as supervision to train a network to detect and classify the subcategory of each object. Subcategory information is then transferred to obtain the pose of each object. More recently, Chabot et al. [12] create a dataset of 3D shapes and templates, and identify the most similar template for each object that is detected. To do so, they manually

annotate vehicle part coordinates, part visibility and the 3D template corresponding to each object in the training set. At test time, their network predicts all part coordinates, their visibility and the most similar template. A 2D/3D matching algorithm (Perspective-n-Point) then produces the desired object pose. These methods generally provide more information about each object, at the expense of having a more convoluted approach involving a database of shapes, templates, voxel patterns etc., and sometimes requiring more manual annotations.

Archetypal studies that make use of 3D object proposals for monocular detection are presented by Chen et al. in [13, 14]. In these studies, the authors first sample candidate 3D boxes using a ground plane assumption and object size priors. These boxes are then scored by exploiting different cues like semantic and instance classes, context, shape, location etc. Although these methods work well on 2D detection tasks, they fail to localize objects accurately in 3D.

Unlike previous methods, some recent studies have chosen to enforce geometric constraints to obtain the 6DoF pose of objects. In [15], Mousavian et al. only predict the orientation of objects, and use the fact that the perspective projection of a 3D bounding box should fit tightly within its 2D detection window. In a more straightforward approach, the authors in [16] use a single shot network to predict 2D projections of all 8 corners and the centroid of the 3D bounding box, and use these 2D-3D correspondences to obtain the 6DoF pose of the object by solving the Perspective-n-Point (PnP) problem. These methods, although conceptually simple and straightforward to implement, rely on the accuracy of all predicted entities.

3. Network Architecture

3.1. Overview

Our primary focus in this study is to propose an approach to real time 3D object detection for the purpose of autonomous driving. With this in mind, our network design is based on the RetinaNet detector presented in [7]. Although our approach can be adapted to work with any generic object detector based on anchor boxes, we decided to work with the RetinaNet architecture because it matches the speed of other one-stage detectors, while having comparable performance to state-of-the-art two stage detectors. As illustrated in Figure 2, we retain the backbone structure based on Feature Pyramid Networks (FPN) [17], and modify and add to the subnetworks that follow. For most of our experiments, we use a ResNet50 backbone [18] with five pyramid levels (P_3 to P_7) computed using convolutional features C_3 , C_4 and C_5 from the ResNet architecture as before. However, unlike [7], all pyramid levels have $C = 512$ channels instead of 256 to account for the increase in the

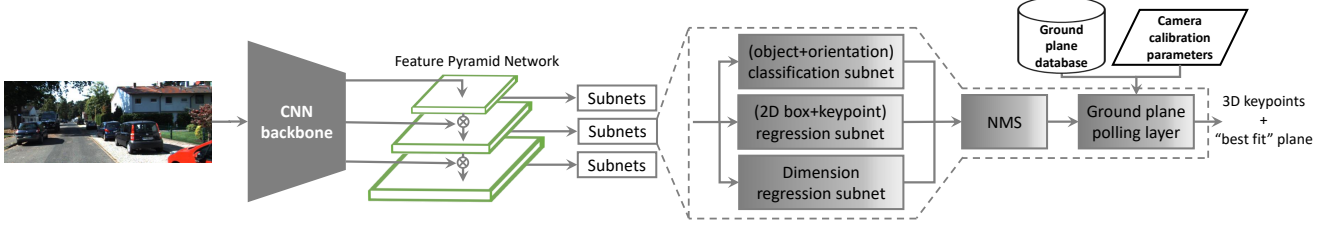


Figure 2: Network architecture and our overall approach for predicting 3D bounding boxes from monocular images.

number of subnetwork outputs, and the number of channels per output. We describe the purpose and structure of each subnetwork in the subsections that follow. Details of the ground plane polling layer are presented in the following section.

3.2. Subnetwork Architectures

(object + orientation) classification subnet: This subnetwork is similar to the classification head found in 2D detectors, with the notable addition of orientation classes. In particular, we define 4 coarse orientation classes tied to 4 different ranges into which an object’s yaw angle in the camera coordinate frame may fall. These orientation classes and the corresponding change in object appearance is depicted in Figure 3. In this Figure, each vertical edge of the 3D bounding box is color coded to indicate its relationship to the orientation classes. Each orientation class is further split into two classes depending on the relative locations of certain keypoints of interest with respect to the center of each anchor. This yields a total of 8 orientation classes. We explain the nature of these split classes in our description of the regression subnetwork.

The classification subnetwork architecture is then modified to predict not just the object class, but also the desired orientation class. As can be seen in Figure 4, this subnetwork takes in the output from each level of the FPN, applies a series of convolutional operations resulting in an output with $8KA$ channels to account for each of 8 orientation classes, K object classes, and A anchors per location. We use a focal loss [7] to train this subnetwork:

$$L_{class}(\mathbf{p}, \mathbf{y}) = - \sum_{k=1}^K \sum_{o=1}^8 \alpha_{k,o} (1 - \mathbf{p}_{k,o})^\gamma \mathbf{y}_{k,o} \log(\mathbf{p}_{k,o}), \quad (1)$$

where \mathbf{p} and \mathbf{y} are the estimated probabilities and one-hot ground truth vector corresponding to positive and negative anchors. The total classification loss is summed across all positive and negative anchors, and is normalized by the total number of positive anchors.

(2D box + keypoint) regression subnet: This subnetwork is used to regress to not only the desired 2D detection box,

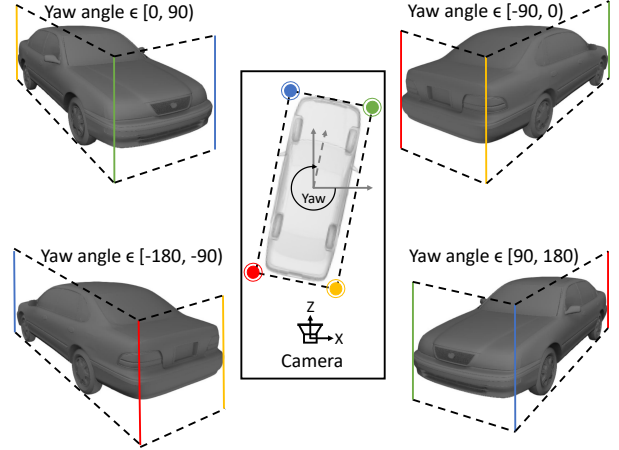


Figure 3: Illustration of the 4 different orientation classes based on yaw angles (corners of the figure), and a bird’s-eye view of how the yaw angle is calculated (center of the figure). Best viewed in color.

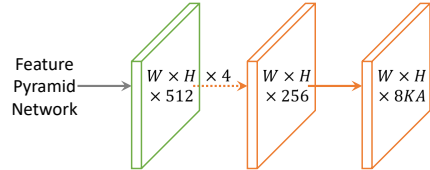


Figure 4: **(object+orientation) classification subnet:** output channels accounts for 8 orientation classes, per anchor, per object class.

but also four additional keypoints of interest: \mathbf{x}_l , \mathbf{x}_m , \mathbf{x}_r , and \mathbf{x}_t that denote the left, middle, right and top *visible* corners of the desired 3D bounding box when projected into the image plane. We perform class and orientation agnostic regression for both the 2D boxes and the keypoints. This implies that a given keypoint may represent different corners of the 3D bounding box depending on the orientation class of the object in question.

Figure 5 outlines the different regression targets for each

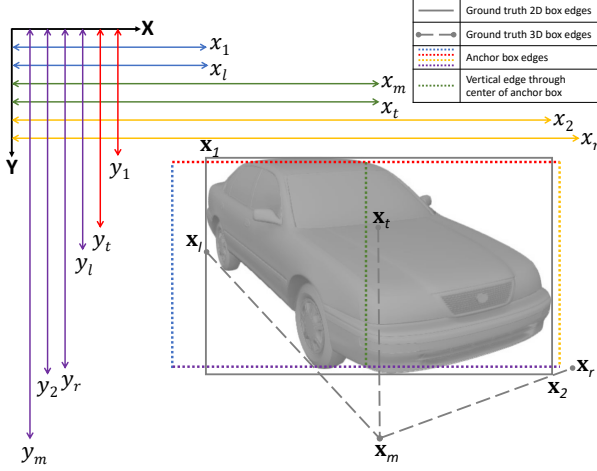


Figure 5: Illustration of proposed regression targets for each anchor. Each target is colored based on the anchor edge from which it is regressed. Best viewed in color.

positive anchor, and also the edge of the anchor from which each target is regressed. The subnetwork architecture and its outputs are depicted in Figure 6. Each keypoint location and the 2D box are predicted through separate heads to force the predictions to be less correlated. Doing so is important to ensure that the predictions are more independent, and to reduce common failure modes of multiple predictions. This helps build a better consensus set during ground plane polling (described in Section 4.2).

Finally, for the X coordinates x_m and x_t of keypoints \mathbf{x}_m and \mathbf{x}_t , we only regress to the absolute values of the target (see Figure 6). The corresponding signs of these regression targets for each anchor are accounted for by the split in orientation classes described in the classification subnetwork i.e. for each anchor, the classification network picks one of 8 orientation classes, which both defines the coarse orientation of the object, and the sign of the regression targets for x_t and x_m . This is especially important for degenerate vehicle orientations close to the boundaries of different orientation classes.

We use a smooth $L1$ loss for all regression heads. The total loss for each positive anchor in this subnetwork is the sum of all individual losses:

$$L_{reg}(\tilde{\mathbf{t}}, \mathbf{t}) = L_{smooth-L1}(\tilde{\mathbf{t}}_{2D}, \mathbf{t}_{2D}) + L_{smooth-L1}(\tilde{\mathbf{t}}_{\mathbf{x}_l}, \mathbf{t}_{\mathbf{x}_l}) \\ + L_{smooth-L1}(\tilde{\mathbf{t}}_{\mathbf{x}_m}, \mathbf{t}_{\mathbf{x}_m}) + L_{smooth-L1}(\tilde{\mathbf{t}}_{\mathbf{x}_r}, \mathbf{t}_{\mathbf{x}_r}) \\ + L_{smooth-L1}(\tilde{\mathbf{t}}_{\mathbf{x}_t}, \mathbf{t}_{\mathbf{x}_t}), \quad (2)$$

where $\tilde{\mathbf{t}}$ and \mathbf{t} are the regression outputs and the corresponding targets respectively. The total loss for this subnetwork is the average loss over all positive anchors.

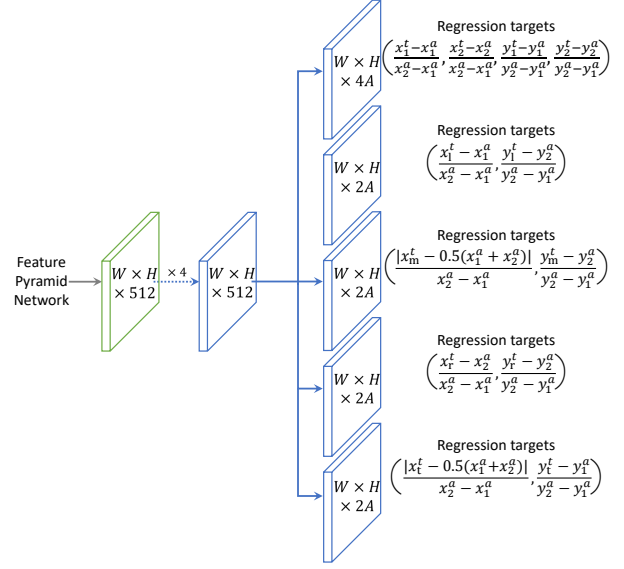


Figure 6: **(2D box+keypoint) regression subnet:** we use separate heads for the 2D box and each keypoint. All regression targets associated with a target bounding box $(x_1^t, x_2^t, y_1^t, y_2^t)$, its keypoints $\{(x_l^t, y_l^t), (x_m^t, y_m^t), (x_r^t, y_r^t), (x_t^t, y_t^t)\}$, and a positive anchor $(x_1^a, x_2^a, y_1^a, y_2^a)$ are shown for reference.

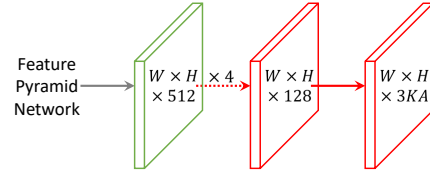


Figure 7: **Dimension regression subnet:** output channels accounts for three dimensions (height, width, length), per anchor, per object class.

Dimension regression subnet: This subnetwork has a similar architecture to the (object + orientation) classification subnetwork, but with fewer channels (128 instead of 256) per convolution. The network directly outputs the three dimensions (height, width, length) of the desired 3D bounding box, but in a class specific manner. By making the predictions class specific, we improve the prediction accuracies just by reducing the variance within each class. The subnetwork architecture is shown in Figure 7, resulting in an output with $3KA$ channels.

The dimension regression subnetwork is trained using a smooth $L1$ loss:

$$L_{dim}(\tilde{\mathbf{d}}, \mathbf{d}) = L_{smooth-L1}(\tilde{\mathbf{d}}, \mathbf{d}), \quad (3)$$

where $\tilde{\mathbf{d}}$ and \mathbf{d} are the regression outputs and the corresponding targets for all three dimensions respectively. The total loss for this subnetwork is average loss over all positive anchors.

The final loss for the entire network is a weighted sum of the three subnetwork losses:

$$L = L_{class} + \lambda_{reg} L_{reg} + \lambda_{dim} L_{dim}. \quad (4)$$

4. Ground Plane Identification by Polling

4.1. Database Creation

As highlighted in Figure 2, the ground plane polling block takes in a database of probable ground planes and outputs the “best fit” plane for each detection. This database of planes can be compiled either using heuristics based on the camera location, or by using 3D sensors like LiDARs to automatically fit planes to 3D data. In this study, we adopt the latter approach. In particular, we make use of the KITTI-15 dataset [19] comprising of 200 RGB images, LiDAR point clouds, and pixel-accurate semantic labels.

Algorithm 1 describes the approach to creating a ground plane database using such data. The procedure involves identifying and retaining LiDAR points corresponding to semantic classes of interest, and then iteratively fitting planes to these points using RANSAC. Since we are interested in generating a large number of diverse ground planes, we use a very small inlier threshold ($t = 2cm$) and a very high probability of success ($p = 0.999$). This produces approximately 22k ground plane candidates.

4.2. Ground Plane Polling

Given a ground plane and 2D keypoints \mathbf{x}_l , \mathbf{x}_m , and \mathbf{x}_r of an object, it is straightforward to obtain the corresponding 3D keypoints lying on the plane. This is done by backprojecting a ray from the camera center through each keypoint, and finding its point of intersection with the plane. The backprojected ray $\mathbf{r} = (r_1, r_2, r_3, r_4)^T$ for a 2D keypoint $\mathbf{x} = (x, y)^T$ is created using the camera projection matrix,

$$\mathbf{r} = P^+[x, y, 1]^T, \quad (5)$$

and the corresponding 3D keypoint on the plane $\pi = (a, b, c, d)^T$ is given by

$$\mathbf{X}^\pi = s[r_1, r_2, r_3]^T, \quad (6)$$

where the scalar s is defined as follows

$$s = \frac{-dr_4}{ar_1 + br_2 + cr_3}. \quad (7)$$

This results in the 3D keypoints \mathbf{X}_l^π , \mathbf{X}_m^π , \mathbf{X}_r^π corresponding to 2D keypoints \mathbf{x}_l , \mathbf{x}_m , \mathbf{x}_r , lying on the plane π .

Unlike the other three keypoints, the desired point \mathbf{X}_t^π corresponding to the 2D keypoint \mathbf{x}_t does not lie on the

Algorithm 1 Pseudocode for creating a database of ground planes

Inputs: $\{im_i^{seg}\}_{i=1}^N$ \triangleright ground truth semantic segmentation
 $\{(X_i^j, Y_i^j, Z_i^j)\}_{j=1}^M$ \triangleright LiDAR point cloud
 $P_i\}_{i=1}^N$ \triangleright camera calibration matrix
 $semantic_classes = \{ground, road, sidewalk, parking\}$
 \triangleright semantic classes of interest

Outputs: $\{\pi_k\}_{k=1}^K$ \triangleright database of ground planes

```

ground_planes  $\leftarrow \{\}$ 
for  $i \leftarrow 1$  to  $N$  do
  points  $\leftarrow \{\}$ 
  for  $j \leftarrow 1$  to  $M$  do
     $(x_i^j, y_i^j) \leftarrow project((X_i^j, Y_i^j, Z_i^j), P_i)$ 
     $\triangleright$  project LiDAR point to image plane
    if  $im_i^{seg}(x_i^j, y_i^j) \in semantic\_classes$  then
      points  $\leftarrow points \cup \{(X_i^j, Y_i^j, Z_i^j)\}$ 
    end if
  end for
  while  $|points| \geq 3$  do
     $\pi, inliers \leftarrow RANSAC(points)$ 
    ground_planes  $\leftarrow ground\_planes \cup \{\pi\}$ 
    points  $\leftarrow points \setminus inliers$ 
  end while
end for
return ground_planes

```

plane π , but is rather a point on the line through \mathbf{X}_m^π along the normal to the plane π . Since the desired 3D keypoint lies on both the backprojected ray \mathbf{r} and the plane normal through \mathbf{X}_m^π , we could ideally calculate it from the intersection of these two lines. In practice, however, these are skew lines that do not intersect. We therefore resort to an approximation, where \mathbf{X}_t^π is designated as the point on the plane normal through \mathbf{X}_m^π that is closest in distance to the ray \mathbf{r} . If \mathbf{n}_r and \mathbf{n}_π are the unit vectors representing the directions of the ray \mathbf{r} and the plane normal respectively, the desired point can be calculated as follows:

$$\mathbf{X}_t^\pi = \mathbf{X}_m^\pi - \frac{\mathbf{X}_t^\pi \cdot (\mathbf{n}_r \times (\mathbf{n}_\pi \times \mathbf{n}_r))}{\mathbf{n}_\pi \cdot (\mathbf{n}_r \times (\mathbf{n}_\pi \times \mathbf{n}_r))} \mathbf{n}_\pi. \quad (8)$$

To find out how well a ground plane π fits the predicted 2D keypoints and 3D dimensions of an object, we propose an approach based on the construction of triplets comprised of two 3D keypoints, and the estimated length of the line segment joining them. Four 3D keypoints result in a total of ${}^4C_2 = 6$ unique pairs of keypoints, and therefore 6 total triplets $\{(\mathbf{X}_i^\pi, \mathbf{X}_{i'}^\pi, l_i)\}_{i=1}^6$. Note that the lengths of the line segments are determined using the 3D box dimensions predicted by the network.

Each triplet $(\mathbf{X}_i^\pi, \mathbf{X}_{i'}^\pi, l_i)$ is associated with a residual error defined by:

$$e_i^\pi = |||\mathbf{X}_i^\pi - \mathbf{X}_{i'}^\pi|| - l_i|, \quad (9)$$

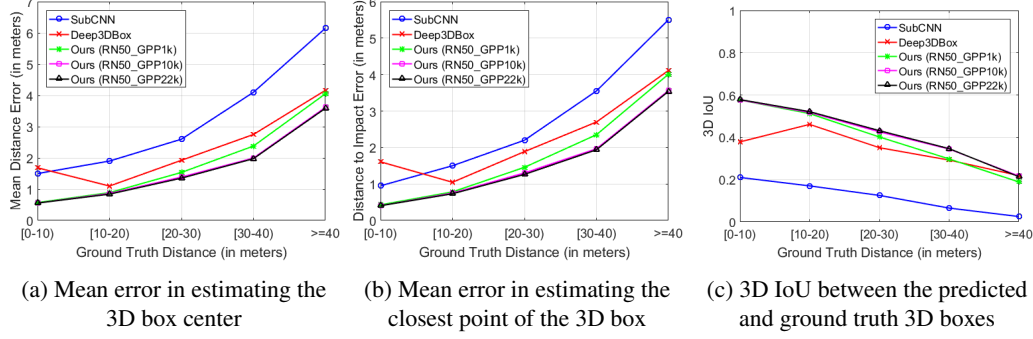


Figure 8: Comparison of 3D metrics for different approaches on KITTI cars using the validation set provided in [11, 15].

and the total residual error e^π for a plane is the sum of the six individual errors. Finally, the “best fit” ground plane for a given object from a database of probable ground planes $\{\pi_k\}_{k=1}^K$ is determined to be

$$\pi^* = \arg \min_{\pi_k \in \{\pi_k\}_{k=1}^K} \sum_{i=1}^6 e_i^{\pi_k}. \quad (10)$$

The residual errors tied to the three dimensions of the bounding box ensure that a plane that produces a box of reasonable dimensions is chosen. The other three errors corresponding to the face diagonals of the bounding box promote planes that result in boxes with nearly orthogonal edges. In our experiments, directly enforcing orthogonality or near-orthogonality led to most probable planes being discarded, thereby causing performance degradation.

Knowing the “best fit” plane π^* , we first discard one of the three keypoints ($\mathbf{X}_l^{\pi^*}$, $\mathbf{X}_m^{\pi^*}$, $\mathbf{X}_r^{\pi^*}$) with highest reprojection error (note that each keypoint can be calculated using the other two keypoints and object dimensions by assuming orthogonality, which can then be projected into the image to determine the associated reprojection error). Next, we construct the desired 3D cuboid by utilizing the other two keypoints, the estimated 3D dimensions and the predicted orientation class. To account for a large database of ground planes, potentially large number of objects per image, and to leverage the GPU for matrix multiplications, we implement the entire polling procedure as a layer in our network. This layer is referred to as the ground plane polling (GPP) layer.

5. Experimental Evaluation

5.1. Implementation Details

Training: We use $\gamma = 2$ and $\alpha = 0.25$ for the focal loss presented in Equation 1. The backbone of our network is pre-trained on ImageNet1k. The total loss depicted in Equation 4 is fairly robust to the choice of hyperparameters λ_{reg} and λ_{dim} provided the network is trained for enough

epochs. We set $\lambda_{reg} = \lambda_{dim} = 1$ for simplicity. The entire network is trained using mini-batch gradient descent using an Adam optimizer with learning rate 0.00001, $\beta_1 = 0.9$ and $\beta_2 = 0.999$. We use a batch size of two images and train for a total of 70 epochs on a single GPU. We also resorted to both geometric and pixel intensity transformations for data augmentation. We apply random rotations in the image plane, translations, shears, scalings and horizontal flips to input images for robustness against small geometric transformations. Additionally, the brightness, contrast, saturation and hue of input images were randomly perturbed.

Inference: During inference, we add the NMS and GPP layers to the end of the subnetwork outputs at each level of the FPN. To ensure fast operation, we only decode box predictions from at most 1k top-scoring predictions per FPN level, after thresholding detector confidence at 0.05. The top predictions from all levels are merged and non-maximum suppression with a threshold of 0.5 is applied to yield the final 2D detections. These detections and their corresponding keypoints, dimensions and orientations are passed on to the GPP layer, which outputs the 3D keypoints and “best fit” ground plane for each detection. The desired 3D bounding box is then constructed using these outputs.

5.2. Results

Evaluation of 3D bounding box metrics: The KITTI detection and orientation estimation benchmark for cars only evaluates the partial pose of vehicles. To provide a more complete evaluation and comparison with other monocular methods, we carry out analogous experiments to the ones proposed in [15]. In particular, we plot three metrics of interest as a function of the distance of an object from the camera. The first metric is the average error in estimating the 3D coordinate of the center of objects. The second metric is the average error in estimating the closest point of the 3D bounding box from the camera. The last metric is the standard 3D intersection over union (3D IoU) that depends on all factors of the 3D bounding box.

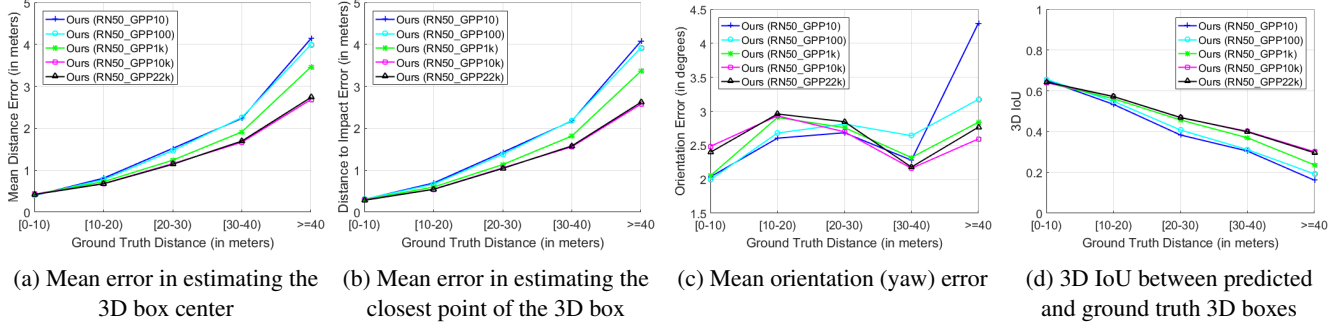


Figure 9: Effect of ground plane database size on 3D bounding box metrics for KITTI cars on a common validation set.

Table 1: **Results on the KITTI benchmark:** Comparison of the Average Orientation Similarity (AOS), Average Precision (AP) and Orientation Score (OS) for cars. Our runtimes are reported using a Titan X Maxwell GPU @ 1.0GHz base clock.

Method	Runtime (seconds)	Easy			Moderate			Hard		
		AOS	AP	OS	AOS	AP	OS	AOS	AP	OS
DeepMANTA [12]	2.00	96.32%	96.40%	0.9991	89.91%	90.10%	0.9979	80.55%	80.79%	0.9970
Mono3D [14]	4.20	91.01%	92.33%	0.9984	86.62%	88.66%	0.9769	76.84%	78.96%	0.9731
SubCNN [11]	2.00	90.67%	90.81%	0.9984	88.62%	89.04%	0.9952	78.68%	79.27%	0.9925
Deep3DBox [15]	1.50	92.90%	92.98%	0.9991	88.75%	89.04%	0.9967	76.76%	77.17%	0.9946
Ours (RN50_GPP10k)	0.21	89.28%	89.49%	0.9977	85.89%	86.86%	0.9888	76.30%	77.48%	0.9848
Ours (RN101_GPP10k)	0.24	89.57%	89.76%	0.9979	86.46%	87.36%	0.9897	77.04%	78.24%	0.9847
Ours (VGG16_GPP10k)	0.19	88.98%	89.08%	0.9989	86.98%	87.37%	0.9955	77.45%	78.10%	0.9917
Ours (VGG19_GPP10k)	0.23	90.14%	90.22%	0.9991	87.79%	88.06%	0.9969	78.51%	78.95%	0.9945

In keeping with the original experiment, we factor away the 2D detection performance by considering only those detections that result in an $\text{IoU} \geq 0.7$ with the ground truth 2D box. This removes the effects of 2D detection performance and enables a side-by-side comparison of how well each method performs on the desired 3D metrics. To make the comparison fair, we use the same *train-val* split provided in [11], where the KITTI training dataset comprising of 7481 images is split into a *train* and *val* sets consisting of 3619 and 3799 images respectively. We compare our method to current (Deep3DBox [15]) and previous (SubCNN [11]) state-of-the-art monocular methods with publicly available results and code. We compare three variants of our method: RN50_GPP1k, RN50_GPP10k and RN50_GPP22k, all three of which have a ResNet50 backbone, and differ only by the size of the ground plane database used in the GPP layer (1k, 10k and 22k planes respectively). As Figure 8 shows, all three variants of our method outperform the other two methods on nearly all data points in the plot despite being an order of magnitude faster.

Effect of ground plane database size: To quantify the effect of the number of ground planes used in the database, we provide comparative analysis of different variants of our method using the same 3D metrics as before. Additionally, we also plot the orientation error (in degrees) averaged across all samples as a function of distance to the cam-

era. Crucially, we create a different *train-val* split to ensure that the network does not overfit, leading to a more accurate comparison. The resulting *train* and *val* sets consist of 6373 and 1108 images respectively. Each set is comprised of images from disparate drives with no overlap.

As mentioned in Section 4.1, our complete database is made of 22k candidate ground planes. To create databases of smaller sizes, we rank planes based on the number of inliers associated with them (see Algorithm 1), and choose planes in a “top-k” fashion. While retaining the same ResNet50 backbone and sub-networks, we provide comparisons between databases of size 10, 100, 1k, 10k and 22k. We refer to these 5 variants as RN50_GPP10, RN50_GPP100, RN50_GPP1k, RN50_GPP10k and RN50_GPP22k respectively.

Figure 9 depicts the comparison between these variants on all four metrics. As expected, we see an increase in performance over all metrics as the size of the ground plane database is increased. This effect is exacerbated as the distance of objects from the camera increases. The plots also seem to indicate that doubling the number of planes from 10k to 22k results in minor performance improvement, and even degradation in some cases. This hints at a case of diminishing returns beyond a database with 10k ground planes. With this in mind, we use a database of 10k ground planes as our default choice in other experiments.

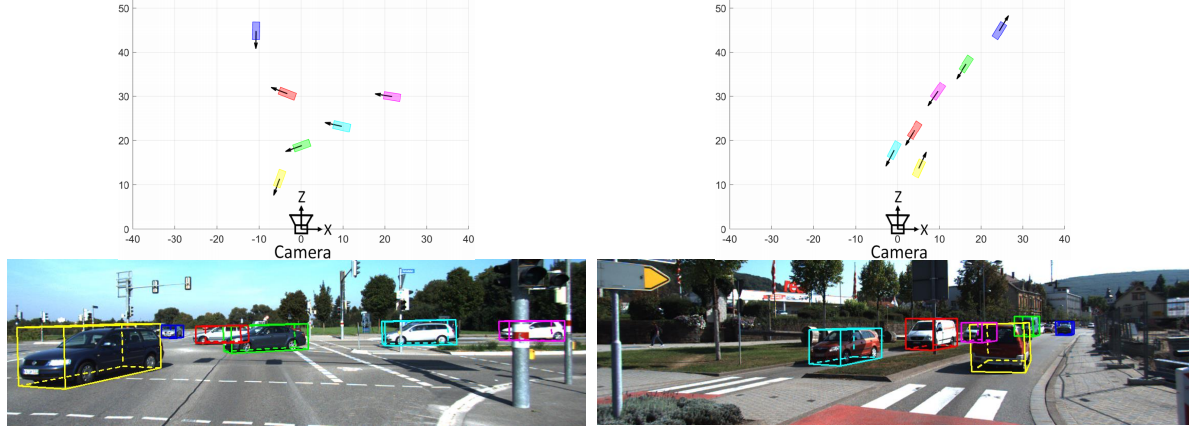


Figure 10: **Qualitative results on the KITTI test set:** We show both the bird’s eye view of the predicted boxes (top), and their corresponding projections onto the input image (bottom). Each 3D box is color coded to represent unique cars.

KITTI 2D detection and orientation benchmark: The official 3D metric of the KITTI dataset is Average Orientation Similarity (AOS), which is defined in [3] and multiplies the average precision (AP) of the 2D detector with the average cosine distance similarity for the azimuth. Hence, AP is by definition the upper bound of AOS. Our results are summarized in Table 1, along with other top entries on the KITTI leaderboard. Since the AP and AOS metrics are heavily influenced by the 2D detection performance, we additionally list the ratio of AOS over AP for each method as done in previous works. This ratio is representative of how each method performs only on orientation estimation, while factoring out the 2D detector performance.

A cursory glance at Table 1 indicates that our model is mostly within a few precision points of other methods in terms on AP and AOS. This is expected given that our method is the only single-stage approach that does not require object proposals of any kind, thereby resulting in a speedup not possible with other multi-stage methods. More importantly, our best performing model (with a VGG19 backbone) only falls behind DeepMANTA [12] by a small amount on the OS score, while beating out or remaining at par with other methods. We manage to do so at a fraction of the computational cost, and without requiring additional annotations associated with keypoints, part labels, and part visibility as needed in DeepMANTA. Additionally, our method is the only one that does not rely on computing additional features such as stereo, semantic segmentation, instance segmentation, etc., and does not need preprocessing as in [12, 14, 15]. To further demonstrate the robustness of our GPP approach, we show some qualitative results of our method on the KITTI test set in Figure 10.

Effect of different backbones: To observe the effect of dif-

ferent backbone sizes and architectures on the final result, we provide results for four popular backbone choices on the KITTI benchmark in Table 1. We refer to these variants as RN50_GPP10k, RN101_GPP10k, VGG16_GPP10k and VGG19_GPP10k, each named after the corresponding backbone architecture used. The FPN for the two VGG architectures [20] are constructed using the features from the maxpooling layers P_3 , P_4 , and P_5 that follow the convolutional blocks C_3 , C_4 , and C_5 respectively. Surprisingly, the smaller VGG backbones yield better results, especially for orientation-related metrics. The larger VGG19 backbone even results in superior AP across the board, and is therefore our best performing model. The RN101 backbone leads to a meager improvement in comparison to the smaller RN50 backbone, implying that adding more layers does not necessarily justify the return. We believe that the superior performance of the VGG variants is most likely explained by their use of smaller convolutional kernels, which preserves smaller details, resulting in better keypoint predictions.

6. Conclusion

In this study, we introduce an approach to monocular 3D object detection using a single-shot CNN. The approach is capable of predicting the 6DoF pose and 3D dimensions of objects on the road by merging 2D attributes like keypoints and coarse orientations with 3D information from probable ground plane configurations. By doing so, we also ensure that our network only predicts those entities that are known to generalize well across different conditions and datasets. Adapting to a new dataset would only involve reassessing the database of 3D ground planes. Additionally, our approach produces a redundant set of cues and relies on identifying a suitable consensus set within, thereby resulting in robustness to individual errors and outliers. We have shown

that our GPP approach significantly outperforms other popular monocular approaches in terms of localization, while remaining comparable to other methods in 2D detection performance. Most importantly, our approach achieves this with a significantly smaller inference time. Future work entails adopting our approach to recent two-stage detectors, and also conducting experiments to analyze its robustness to prediction errors and generalizability to other datasets.

References

- [1] A. Rangesh and M. M. Trivedi, “No blind spots: Full-surround multi-object tracking for autonomous vehicles using cameras & lidars,” *arXiv preprint arXiv:1802.08755*, 2018. [1](#)
- [2] N. Deo, A. Rangesh, and M. M. Trivedi, “How would surround vehicles move? a unified framework for maneuver classification and motion prediction,” *IEEE Transactions on Intelligent Vehicles*, vol. 3, no. 2, pp. 129–140, 2018. [1](#)
- [3] A. Geiger, P. Lenz, and R. Urtasun, “Are we ready for autonomous driving? the kitti vision benchmark suite,” in *Conference on Computer Vision and Pattern Recognition (CVPR)*, 2012. [2, 8](#)
- [4] Y. Xiang, R. Mottaghi, and S. Savarese, “Beyond pascal: A benchmark for 3d object detection in the wild,” in *Applications of Computer Vision (WACV), 2014 IEEE Winter Conference on*. IEEE, 2014, pp. 75–82. [2](#)
- [5] K. Matzen and N. Snavely, “Nyc3dcars: A dataset of 3d vehicles in geographic context,” in *Proceedings of the IEEE International Conference on Computer Vision*, 2013, pp. 761–768. [2](#)
- [6] J. Redmon, S. Divvala, R. Girshick, and A. Farhadi, “You only look once: Unified, real-time object detection,” in *Proceedings of the IEEE conference on computer vision and pattern recognition*, 2016, pp. 779–788. [2](#)
- [7] T.-Y. Lin, P. Goyal, R. Girshick, K. He, and P. Dollár, “Focal loss for dense object detection,” *IEEE transactions on pattern analysis and machine intelligence*, 2018. [2, 3](#)
- [8] S. Ren, K. He, R. Girshick, and J. Sun, “Faster r-cnn: Towards real-time object detection with region proposal networks,” in *Advances in neural information processing systems*, 2015, pp. 91–99. [2](#)
- [9] F. Yang, W. Choi, and Y. Lin, “Exploit all the layers: Fast and accurate cnn object detector with scale dependent pooling and cascaded rejection classifiers,” in *Proceedings of the IEEE conference on computer vision and pattern recognition*, 2016, pp. 2129–2137. [2](#)
- [10] Y. Xiang, W. Choi, Y. Lin, and S. Savarese, “Data-driven 3d voxel patterns for object category recognition,” in *Proceedings of the IEEE Conference on Computer Vision and Pattern Recognition*, 2015, pp. 1903–1911. [2](#)
- [11] —, “Subcategory-aware convolutional neural networks for object proposals and detection,” in *Applications of Computer Vision (WACV), 2017 IEEE Winter Conference on*. IEEE, 2017, pp. 924–933. [2, 6, 7](#)
- [12] F. Chabot, M. Chaouch, J. Rabarisoa, C. Teulière, and T. Chateau, “Deep manta: A coarse-to-fine many-task network for joint 2d and 3d vehicle analysis from monocular image,” in *Proc. IEEE Conf. Comput. Vis. Pattern Recognit.(CVPR)*, 2017, pp. 2040–2049. [2, 7, 8](#)
- [13] X. Chen, K. Kundu, Y. Zhu, A. G. Berneshawi, H. Ma, S. Fidler, and R. Urtasun, “3d object proposals for accurate object class detection,” in *Advances in Neural Information Processing Systems*, 2015, pp. 424–432. [2](#)
- [14] X. Chen, K. Kundu, Z. Zhang, H. Ma, S. Fidler, and R. Urtasun, “Monocular 3d object detection for autonomous driving,” in *Proceedings of the IEEE Conference on Computer Vision and Pattern Recognition*, 2016, pp. 2147–2156. [2, 7, 8](#)
- [15] A. Mousavian, D. Anguelov, J. Flynn, and J. Košecká, “3d bounding box estimation using deep learning and geometry,” in *Computer Vision and Pattern Recognition (CVPR), 2017 IEEE Conference on*. IEEE, 2017, pp. 5632–5640. [2, 6, 7, 8](#)
- [16] B. Tekin, S. N. Sinha, and P. Fua, “Real-time seamless single shot 6d object pose prediction,” *arXiv preprint arXiv:1711.08848*, 2017. [2](#)
- [17] T.-Y. Lin, P. Dollár, R. B. Girshick, K. He, B. Hariharan, and S. J. Belongie, “Feature pyramid networks for object detection,” in *CVPR*, vol. 1, no. 2, 2017, p. 4. [2](#)
- [18] K. He, X. Zhang, S. Ren, and J. Sun, “Deep residual learning for image recognition,” in *Proceedings of the IEEE conference on computer vision and pattern recognition*, 2016, pp. 770–778. [2](#)
- [19] H. Alhaija, S. Mustikovela, L. Mescheder, A. Geiger, and C. Rother, “Augmented reality meets computer vision: Efficient data generation for urban driving scenes,” *International Journal of Computer Vision (IJCV)*, 2018. [5](#)
- [20] K. Simonyan and A. Zisserman, “Very deep convolutional networks for large-scale image recognition,” *arXiv preprint arXiv:1409.1556*, 2014. [8](#)